The Cryosphere Discuss., 9, 2301–2337, 2015
www.the-cryosphere-discuss.net/9/2301/2015/
doi:10.5194/tcd-9-2301-2015

The Cryosphere Discussions
Open Access

Simulated high-latitude soil thermal dynamics during the past four decades

S. Peng[1,2], P. Ciais[2], G. Krinner[1], T. Wang[1,2], I. Gouttevin[1,3], A. D. McGuire[4], D. Lawrence[5], E. Burke[6], X. Chen[7], C. Delire[8], C. Koven[9], A. MacDougall[10], A. Rinke[11,12], K. Saito[13], W. Zhang[14], R. Alkama[8], T. J. Bohn[15], B. Decharme[8], T. Hajima[13], D. Ji[11], D. P. Lettenmaier[7], P. A. Miller[14], J. C. Moore[11], B. Smith[14], and T. Sueyoshi[13]

[1]UJF–Grenoble 1/CNRS, Laboratoire de Glaciologie et Géophysique de l'Environnement (LGGE), 38041 Grenoble, France
[2]Laboratoire des Sciences du Climat et de l'Environnement (LSCE), CEA-CNRS-UVSQ, 91191 Gif-sur-Yvette, France
[3]Irstea, UR HHLY, 5 rue de la Doua, CS 70077, 69626 Villeurbanne CEDEX, France
[4]US Geological Survey, Alaska Cooperative Fish and Wildlife Research Unit, University of Alaska Fairbanks, Fairbanks, AK, USA
[5]National Center for Atmospheric Research, Boulder, CO, USA
[6]Met Office Hadley Centre, FitzRoy Road, Exeter, EX1 3PB, UK
[7]Department of Civil and Environmental Engineering, University of Washington, Seattle, WA, USA
[8]CNRM-GAME, Unitémixte de recherche CNRS/Meteo-France, UMR 3589, 42 av Coriolis, 31057 Toulouse cedex, France

[9]Lawrence Berkeley National Laboratory, Berkeley, CA, USA
[10]School of Earth and Ocean Sciences, University of Victoria, Victoria, BC, Canada
[11]State Key Laboratory of Earth Surface Processes and Resource Ecology, College of Global Change and Earth System Science, Beijing Normal University, Beijing, China
[12]Alfred Wegener Institute Helmholtz Centre for Polar and Marine Research, Potsdam, Germany
[13]Research Institute for Global Change, Japan Agency for Marine–Earth Science and Technology, Yokohama, Kanagawa, Japan
[14]Department of Physical Geography and Ecosystem Science, Lund University, Sölvegatan 12, 223 62 Lund, Sweden
[15]School of Earth and Space Exploration, Arizona State University, Tempe, AZ, USA

Received: 19 January 2015 – Accepted: 12 March 2015 – Published: 9 April 2015

Correspondence to: S. Peng (shushi.peng@lsce.ipsl.fr)

Published by Copernicus Publications on behalf of the European Geosciences Union.

Abstract

Soil temperature (T_s) change is a key indicator of the dynamics of permafrost. On seasonal and inter-annual time scales, the variability of T_s determines the active layer depth, which regulates hydrological soil properties and biogeochemical processes. On the multi-decadal scale, increasing T_s not only drives permafrost thaw/retreat, but can also trigger and accelerate the decomposition of soil organic carbon. The magnitude of permafrost carbon feedbacks is thus closely linked to the rate of change of soil thermal regimes. In this study, we used nine process-based ecosystem models with permafrost processes, all forced by different observation-based climate forcing during the period 1960–2000, to characterize the warming rate of T_s in permafrost regions. There is a large spread of T_s trends at 20 cm depth across the models, with trend values ranging from 0.010 ± 0.003 to $0.031 \pm 0.005\,^{\circ}\mathrm{C\,yr^{-1}}$. Most models show smaller increase in T_s with increasing depth. Air temperature (T_a) and longwave downward radiation (LWDR) are the main drivers of T_s trends, but their relative contributions differ amongst the models. Different trends of LWDR used in the forcing of models can explain 61 % of their differences in T_s trends, while trends of T_a only explain 5 % of the differences in T_s trends. Uncertain climate forcing contributes a larger uncertainty in T_s trends ($0.021 \pm 0.008\,^{\circ}\mathrm{C\,yr^{-1}}$, mean ± SD) than the uncertainty of model structure ($0.012 \pm 0.001\,^{\circ}\mathrm{C\,yr^{-1}}$), diagnosed from the range of response between different models, normalized to the same forcing. In addition, the loss rate of near-surface permafrost area, defined as total area where the maximum seasonal active layer thickness (ALT) is less than 3 m loss rate is found to be significantly correlated with the magnitude of the trends of T_s at 1 m depth across the models ($R = -0.85$, $P = 0.003$), but not with the initial total near-surface permafrost area ($R = -0.30$, $P = 0.438$). The sensitivity of the total boreal near-surface permafrost area to T_s at 1 m, is estimated to be of -2.80 ± 0.67 million $\mathrm{km^2\,^{\circ}C^{-1}}$. Finally, by using two long-term LWDR datasets and relationships between trends of LWDR and T_s across models, we infer an observation-constrained total boreal near-surface permafrost area decrease comprised between

TCD
9, 2301–2337, 2015

$39 \pm 14 \times 10^3$ and $75 \pm 14 \times 10^3$ km^2 yr^{-1} from 1960 to 2000. This corresponds to 9–18 % degradation of the current permafrost area.

1 Introduction

Arctic permafrost regions store ~ 1300 Pg carbon (C) in the soil, including ~ 1100 Pg C in frozen soil and deposits (Hugelius et al., 2014). Decomposition of these large carbon pools in response to permafrost thawing from future warming is expected to be a positive feedback on climate warming through increased emissions of CO_2 and CH_4 (Khvorostyanov et al., 2008; Schuur et al., 2008; McGuire et al., 2009; Koven et al., 2011; Schaefer et al., 2011). The magnitude of permafrost soil carbon feedbacks on climate depends on the rate of soil carbon decomposition, which is related to permafrost thaw, soil water and temperature changes, the quantity and quality of soil carbon available as a substrate for decomposition, and the concentration of oxygen in the soil, which determines CH_4 vs. CO_2 production ratio (Schuur et al., 2008; Schädel et al., 2014; Elberling et al., 2013). Both the rate of permafrost thaw and the rate of soil carbon decomposition are closely related to soil thermal dynamics (Koven et al., 2011; Schädel et al., 2014; Elberling et al., 2013).

Measurements of active layer depth across circumpolar regions and borehole temperature profiles indicate that active layer thickness on top of boreal permafrost has been increasing in response to the warming that occurred during recent decades in North America, Northern Europe and Russia (e.g. Zhang et al., 2001; Qian et al., 2011; Smith et al., 2005, 2010; Romanovsky et al., 2007, 2010). For example, the borehole record of Alert in Canada (82°301′N, 62°25′W) shows that soil temperature at 9, 15 and 24 m increased at rates of 0.6, 0.4 and 0.2 °C decade^{-1} from 1978 to 2007, respectively (Smith et al., 2012). These observations provide long-term local monitoring of changes in active layer thickness and soil temperature, but the measurement sites are sparse, and their temporal sampling frequency is often low (Romanovsky et al., 2010). Because site measurements cannot document permafrost area loss on a large

TCD
9, 2301–2337, 2015

scale, land surface models including “cold processes”, such as soil freeze–thaw and the thermal and radiative properties of snow, are important tools for quantifying the rate of permafrost degradation on a large scale, and its evolution in response to climate change scenarios.

However, there are large uncertainties in soil thermal dynamics in land surface models (e.g. Koven et al., 2013), and these uncertainties also impact predictions of carbon-cycle feedbacks on climate. To quantify and reduce the uncertainty of modeled T_s, the driving factors of T_s trends need to be investigated. It is also important to distinguish the uncertainty caused by assigned parameter values and model structure from the uncertainty attributable to uncertain climate forcing data.

In this study, nine process-based models that participated in the Permafrost Carbon Network (PCN, www.permafrostcarbon.org) were used (1) to compare trends of simulated T_s at different depths over the boreal permafrost regions during the past four decades and to assess the uncertainty of T_s trends across models, (2) to identify which factors drive trends of permafrost T_s; and (3) to quantify the sensitivity of changes in near-surface permafrost area to warming.

2 Methods

2.1 Models and simulations

The nine land surface models that were used for simulating T_s in permafrost regions organized by Permafrost Carbon Network (PCN, www.permafrostcarbon.org) are listed in Table 1. All the models used finite difference solution of heat equation with phase change to simulate T_s, but models have different soil depths, snow parameterizations, and soil thermal conductivity (Table 1). Three models (CLM, ISBA, UW-VIC) explicitly considered organic soil insulation and six models explicitly considered the effect of water in soil on phase change. All models explicitly considered snow insulation but with different snow layers. The soil thermal conductivity depends on soil moisture in all

TCD
9, 2301–2337, 2015

models. More details can be found in Rawlins et al. (2015) and McGuire et al. (2015). We defined the Northern Hemisphere permafrost spatial domain as the definition in Fig. 1, and the analysis considers three permafrost regions, Boreal North America (BONA), Boreal Europe (BOEU), Boreal Asia (BOAS) (Fig. 1; Brown et al., 1998). We did not include the Tibetan plateau because not all the models covered this region. Hereafter, the term "boreal regions" is used in the following for the sum of the three sub-regions BONA, BOEU and BOAS in Fig. 1.

Following the simulation protocol of the PCN project, nine land surface models performed historical simulations from 1960 to 2000, using different forcing data sets (Table 1). Modelers used different forcing datasets for climate and other model boundary conditions (Table 1). Climate forcing data chosen by each group are presented in Table 1, and the differences in the trend of T_a, precipitation, and radiative forcing are summarized in Figs. S1 and S2 in the Supplement. How differences between these drivers are related to differences of the modeled T_s is discussed in the Results and Discussion section.

To separate the contributions of the trends of four forcing variables: T_a, atmospheric CO_2, precipitation, and LWDR on permafrost thermal dynamics and carbon stocks, six out of the nine models conducted factorial simulations (R01–R04). The ORCHIDEE and JULES performed two additional simulations (R05–R06) to isolate the contribution of LWDR on T_s trends (Tables 2 and 3). In the reference simulation R01, all drivers vary at the same time. In R02 T_a is detrended; in R03 atmospheric CO_2 is set constant to the observed 1960 level of 316 ppmv; In R04 both T_a and precipitation are detrended; in R05 T_a and LWDR are detrended; in R06 T_a, precipitation and LWDR are detrended. Differences between two simulations are used to separate the controlling effect of each driver on T_s, and some of their non-linear interactions.

2.2 Analysis

Modeled monthly T_s at 5, 20, 50, 100, 200 and 300 cm depths in every grid cell of each model were calculated by linear interpolation of T_s between the central depths of two

TCD
9, 2301–2337, 2015

adjacent layers. If the maximum soil depth of a model is larger than 300 cm (which is the case for seven models, except CoLM and JULES), then T_s was not extrapolated to layers deeper than 300 cm (the maximum soil depth of each model is shown in Table 1). For each boreal sub-regions BONA, BOEU, BOAS (Fig. 1) T_s was first averaged over all grid cells and the trend of regional mean T_s (denoted $\dot{T}_s$) was calculated from a linear regression. The statistical significance of $\dot{T}_s$ is evaluated by a t test.

To estimate the uncertainty of $\dot{T}_s$ caused by differenced in the trend of each climate input variable, we regressed $\dot{T}_s$ against the trends of T_a, precipitation and short-wave downward radiation (SWDR) and LWDR, respectively, using the output of R01. The uncertainty of $\dot{T}_s$ attributed to each forcing variable is defined as the resulting range of $\dot{T}_s$ associated to different trends in each forcing variable in the models. To this aim, we regressed $\dot{T}_s$ against forcing variable across the models, and the uncertainty of $\dot{T}_s$ resulting from uncertain forcing data was calculated as the range of $\dot{T}_s$ from the maximum and minimum values of forcing data in the regression equation. Then we define the $\dot{T}_s$ uncertainty attributed to model structure, which reflects the differences in model parameterizations and parameter values, as the uncertainty of $\dot{T}_s$ assuming all models were using the same climate forcing data.

Here, we defined near-surface permafrost as in previous studies (e.g. Schneider von Deimling et al., 2012): near-surface permafrost is defined as where the maximum seasonal thaw depth (i.e., the active layer thickness, ALT) is less than 3 m. The total near-surface permafrost area (NSPA) is the sum of the areas of grid cells that fulfill this condition.

We used monthly LWDR data from CRUNCEP v5.2 (http://dods.extra.cea.fr/data/p529viov/cruncep) and WATCH (Weedon et al., 2011) with a spatial resolution of 0.5° by 0.5° during the period 1960–2000 to derive the trend of LWDR. The CRUNCEP LWDR dataset is derived from CRU TS3.21 and NCEP reanalysis meteorology, and ancillary data sets (e.g. Wei et al., 2013). The WATCH LWDR dataset is derived from ERA-40 reanalysis (Weedon et al., 2011). Because there is no long-term large scale LWDR observation product available, we did an experiment using LWDR from CRUN-

TCD
9, 2301–2337, 2015

CEP and WATCH data to estimate the loss of permafrost area during the period 1960–2000 by an empirical relationship found between the loss of permafrost area and LWDR trends across the seven models.

3 Results and discussion

3.1 Trend in upper-layer soil temperature over boreal regions

The simulated values of $\dot{T}_s$ at 20 cm depth averaged over boreal regions range from $0.010 \pm 0.003\,^{\circ}\mathrm{C\,yr^{-1}}$ (CoLM) to $0.031 \pm 0.005\,^{\circ}\mathrm{C\,yr^{-1}}$ (UVic) during the period 1960–2000 (Fig. 2). Figure 3 shows $\dot{T}_s$ at 20 cm for BONA, BOEU and BOAS regions. Six out of the nine models show the largest $\dot{T}_s$ at 20 cm in BOAS, followed by BONA and the smallest $\dot{T}_s$ at 20 cm in BOEU. The other three models (CoLM, JULES and UW-VIC) show the smallest $\dot{T}_s$ at 20 cm in BOAS. Among the six models with smaller $\dot{T}_s$ at 20 cm in BOEU, we found that $\dot{T}_s$ at 20 cm in BOEU is significantly lower than in BOAS and in BONA ($P < 0.001$, two sample t test). This is also shown in the spatial distribution of $\dot{T}_s$ at 20 cm (Fig. 4). For example, in northern Siberia, T_s at 20 cm increased by more than $0.02\,^{\circ}\mathrm{C\,yr^{-1}}$ in five out of the nine models (ISBA, LPJ-GUESS, MICRO-ESM, ORCHIDEE and UVic) but decreased in two models (CoLM and JULES). All models show an increase of T_s at 20 cm in northern BONA, but this increase is of different magnitude between models (Fig. 4). Six models show significant $\dot{T}_s$ at 20 cm over northern and western Siberia, but all models show non-significant $\dot{T}_s$ at 20 cm over northern BOEU (Fig. 4).

3.2 Attenuation of the trend in soil temperature with soil depth

The trend of T_s in soil layers over 0 to 3 m and soil depth is shown in Fig. 5 for each model. Based on ground soil temperature observation, annual T_s at 1.6 m increased by $0.02–0.03\,^{\circ}\mathrm{C\,yr^{-1}}$ from 1960s to 2000s in Russia (Park et al., 2014). The simulated

TCD
9, 2301–2337, 2015

trend of T_s at 1.6 m in most models are within this range (Fig. S3). Two models (CoLM and JULES) show vertically quasi-uniform $\dot{T}_s$ over the upper 3 m of soil. The seven other models show decreasing values of $\dot{T}_s$ with increasing soil depth, but the vertical gradient of $\dot{T}_s$ varies among them (Fig. 5a). UW-VIC has the largest negative vertical gradient of $\dot{T}_s$ ($-0.0052 \pm 0.0001\,^{\circ}\mathrm{C\,yr^{-1}\,m^{-1}}$), followed by ISBA, MICRO-ESM, ORCHIDEE and UVic ($\sim -0.0030 \pm 0.0003\,^{\circ}\mathrm{C\,yr^{-1}\,m^{-1}}$) and by near-zero vertical gradient of $\dot{T}_s$ in CLM ($-0.0009 \pm 0.0003\,^{\circ}\mathrm{C\,yr^{-1}\,m^{-1}}$) and in LPJ-GUESS ($-0.0014 \pm 0.0000\,^{\circ}\mathrm{C\,yr^{-1}\,m^{-1}}$).

Figure 5b shows the trend of T_s in all soil layers over boreal regions. CLM and UVic show an increase of T_s even at depths deeper than 40 m, but T_s exhibited no changes deeper than 22 m in ORCHIDEE (Fig. 5b). T_s increased in the deepest layer of ISBA (12 m) and MIROC-ESM (14 m), and the depth at which T_s exhibited no changes could not be deduced from these two models. UW-VIC shows a negative trend of T_s (i.e. cooling) at depths deeper than 2.5 m. The trends of T_s in all soil layers over BONA, BOEU and BOAS regions decrease in magnitude with increasing soil depth, but show different vertical gradients. In Fig. S3, vertical gradient of $\dot{T}_s$ are shown to be larger in BONA and BOAS than that in BOEU for most models. Figure 6 shows the spatial distribution of the difference in $\dot{T}_s$ at depths between 20 cm and 3 m. $\dot{T}_s$ at 0.2 m is larger than that at 3 m over most regions in BONA, BOEU and BOAS in seven out of the nine models, exceptions being JULES and CoLM. Generally, boreholes records show that mean annual soil temperature at depths between 10 and 30 m have increased during the last three decades over the circumpolar northern permafrost regions (Osterkamp, 2003; Romanovsky et al., 2010; Smith et al., 2005, 2012; Vaughan et al., 2013). In Alaska, T_s at 20 m from boreholes even increased by $\sim 1\,^{\circ}\mathrm{C}$ between the early 1980s and 2001 (Osterkamp, 2003). The observed value of $\dot{T}_s$ at one of Alert (BH3) boreholes is of $\sim 0.04\,^{\circ}\mathrm{C\,yr^{-1}}$ at ~ 2.5 m depth and nearly zero at ~ 27 m depth during the period 1979–2004 (see Fig. 9 in Smith et al., 2012). Some boreholes (BH1 and BH2) at Alert however still indicated a small warming during the period 1979–2008 (Smith et al., 2012) at 37 m. This suggests that much deeper than currently prescribed maximum soil depth are needed for models to calculate the heat flux into the entire soil

TCD
9, 2301–2337, 2015

profile (Stevens et al., 2007). CoLM, JULES and LPJ-GUESS have too shallow maximum soil depth for the calculation of permafrost soil temperature trends over the last four decades, which makes these models even less realistic for deeper T_s projections over the next century (e.g. Alexeev et al., 2007). Compared to the ground temperature observed to increase at depths deeper than 20 m in boreholes during the past three decades (Vaughan et al., 2013), most models seem to underestimate the penetration of heat into deep soil layers (Fig. 5b). Note that this comparison may be biased because of different periods and climate records between sites and model grid cells. It is also recommended that simulations at site level using in-situ local climate forcing can be compared with temperature profiles of boreholes (Smith et al., 2012) to evaluate why models underestimate the warming of T_s at deeper depths.

3.3 Drivers of trend in soil temperature

We used the sensitivity runs (R02–R06) compared with the reference simulation with all drivers varying together (R01) to separate the effects of T_a, CO_2, precipitation, and LWDR on $\dot{T}_s$ during 1960–2000 (Table 3). Seven of the nine models only provided results from R02, R03 and R04. Except for JULES, all the models show a positive response of T_s to increasing T_a, but with different sensitivities (Table 3). The fraction of the trend of T_s explained by air temperature increase alone (R01–R02) is nearly 100 % in CLM, ISBA and UW-VIC, against only 34, 56 and 67 % in ORCHIDEE, UVic and LPJ-GUESS. The increase of atmospheric CO_2 concentration has almost no effect on the increase of T_s in most models (−5 to +4 % of increase of T_s, Table 3). This is expected since CO_2 has no direct effect on T_s apart from its impact on climate. The only indirect effect of rising CO_2 on T_s trends could result from feedbacks between plant productivity driven by rising CO_2, soil carbon changes and soil thermal properties. For instance, if models include heat production from microbial decomposition of soil organic carbon (Khvorostyanov et al., 2008) or if changes in soil organic carbon from the balance of NPP input and decomposition impact the profile of soil heat conductivity and capacity. In that case, the expected response is that a CO_2 driven increase of productivity

TCD
9, 2301–2337, 2015

will increase soil organic carbon, which will enhance the insulation effect of soil organic carbon in the soil and act lower the trend of T_s (Lawrence et al., 2008; Lawrence and Slater, 2008; Koven et al., 2009). Further, complex changes in the surface energy balance from changes in evapotranspiration under higher CO_2 concentrations can influence soil moisture content and affect T_s trends (e.g. Field et al., 1995). Most models do not have a feedback between soil organic carbon dynamics and soil thermal properties, and the increase in soil organic carbon due to rising CO_2 is relatively small in the models compared to the initial soil organic carbon storage (< 0.1 %). The changes in evapotranspiration because of increasing CO_2 are also relatively small (−3 to +1 %). Therefore, the increased CO_2 concentration has a very small effect on $\dot{T}_s$ from 1960 to 2000.

Precipitation shows an increase in BONA and BOEU and a decrease since 1960 in BOAS in the climate forcing used by most models (Fig. S1b). None of the regional trends of precipitation is significant ($P > 0.05$; except for the UW-VIC drivers). Changes in precipitation alone (R02–R04) are found to cause a negative trend of T_s in CLM, JULES and UW-VIC, no effects in LPJ-GUESS and UVic, and a positive trend in ISBA and ORCHIDEE (Table 3). Increasing winter snow-fall can enhance T_s in winter through snow insulation effect (e.g. Smith et al., 2010; Koven et al., 2013). All models in this study indeed show higher winter T_s where winter snow depth became thicker, but with different magnitudes of snow insulation effects across the models. The snow insulation effects are smaller in ISBA, LPJ-GUESS and UVic than that in the other models. A decrease in snow-fall could contribute a negative trend of T_s in CLM and JULES, and conversely, an increase in snow-fall could enhance T_s in ORCHIDEE (Fig. S4; Table 3). In addition, increased rainfall in summer can cause an increase in evapotranspiration during the growing seasons, which could depress the increase of T_s. Because models did not run simulations where precipitation is detrended only during a specific season, the effects of snowfall trends and growing season precipitation trends that may oppose each other, and cannot be separated in this analysis.

TCD
9, 2301–2337, 2015

LWDR significantly increased since 1960 in all models yet with different trends in the forcing data used by each modeling group ($0.058 \sim 0.200\,W\,m^{-2}\,yr^{-1}$) (Fig. S2a) reflecting the different climate forcing data input. LWDR forcing is mainly from two reanalysis datasets (ERA and NCEP) with corrections (e.g. Weedon et al., 2011; http://dods.extra.cea.fr/data/p529viov/cruncep). ORCHIDEE and JULES performed the simulation R05 with detrended LWDR. The results of R01–R05 allowing to attribute $\dot{T}_s$ to trends of LWDR, indicate that the increase of LWDR explains 56 and 31 % of the trend of T_s since 1960 in ORCHIDEE and JULES, respectively. Increased LWDR provides addtional energy to the surface, and dominates the atmosphere-to-soil energy flux in winter over boreal regions when shortwave radiation is small. Even in summer, LWDR contributes ~ 60 % of total downward radiation (SWDR + LWDR) over boreal regions in CRUNCEP. An increase of LWDR with time thus increases the surface energy input, which accelerates the warming of T_s in case the extra energy is not dissipated by an increase of sensible and latent heat flux. The contribution of changes in LWDR, T_a and other factors on all components of the surface energy budget and on T_s could be further studied by testing models against observations from eddy-flux towers located in permafrost soils.

3.4 Uncertainty of modeled soil temperature trends

The uncertainty of modeled $\dot{T}_s$ at 20 cm is large, as given by the spread of model results ($0.010–0.031\,^{\circ}C\,yr^{-1}$). The uncertainty of $\dot{T}_s$ across the models can be conceptually decomposed into two components, a forcing uncertainty (FU) reflecting how different climate input data used by each modeling group contribute to the spread of $\dot{T}_s$ (Table 1), and a structural uncertainty (SU) related to uncertain parameter values and different equations and parameterizations of processes in models. Since T_a and LWDR are the two main drivers of the increase of T_s in most of the models (Sect. 3.3), we regressed $\dot{T}_s$ during 1960–2000 against the trends of T_a and LWDR, in order to estimate the FU. We then estimated SU from the uncertainty of parameters in the regression equation for a normalized same climate forcing across all models.

TCD
9, 2301–2337, 2015

We found no significant correlation between $\dot{T}_a$ and $\dot{T}_s$ over boreal regions or sub-regions across the nine models (Figs. 7 and S5), indicating that a bias of $\dot{T}_a$ forcing is not simply associated with the bias of $\dot{T}_s$ in a particular model compared to the others. We also found that trends of SWDR and precipitation do not significantly explain differences in $\dot{T}_s$ at 20 cm across the models ($P > 0.05$; 21 and 19 % explanation of differences in $\dot{T}_s$ at 20 cm for trends of SWDR and precipitation respectively; Fig. S6). The correlations between trends in winter snow-fall and trends of annual or winter T_s at 20 cm are not significant ($P > 0.05$) across the models for boreal regions or sub-regions. However, the trend of LWDR (L$\dot{W}$DR) can explain 61 % of the differences in $\dot{T}_s$ at 20 cm across the models (Fig. 8). This result indicates that, across the model ensemble, differences of $\dot{T}_s$ at 20 cm between models are positively correlated (R = 0.78, P = 0.037) with differences of L$\dot{W}$DR used by the different modeling groups. $\dot{T}_s$ at 1 m also significantly correlated with L$\dot{W}$DR (R = 0.79, P = 0.034) across the models. The values of L$\dot{W}$DR used by different models averaged over permafrost regions, range from 0.058 to 0.200 $\mathrm{W\,m^{-2}\,yr^{-1}}$, statistically explaining a range of simulated $\dot{T}_s$ at 20 cm of $0.021 \pm 0.005\,^{\circ}\mathrm{C\,yr^{-1}}$ (solid blue arrow in Fig. 8). This $\dot{T}_s$ range defines the FU (the range of $\dot{T}_s$ to L$\dot{W}$DR from 0.058 to 0.200 $\mathrm{W\,m^{-2}\,yr^{-1}}$ based on the linear regression of Fig. 8). We also used multiple linear regression between $\dot{T}_s$ at 20 cm depth and $\dot{T}_a$, L$\dot{W}$DR as independent variables across the models, to derive an estimation of the FU on $\dot{T}_s$ of $0.021 \pm 0.008\,^{\circ}\mathrm{C\,yr^{-1}}$ (the deviation was derived from the uncertainty of regression coefficients in the multiple linear regression). However, the uncertainty of the linear regression of $\dot{T}_s$ at 20 cm by L$\dot{W}$DR or $\dot{T}_a$ and L$\dot{W}$DR shows that if all the models used the same climate forcing data, the SU would be of $0.012 \pm 0.001\,^{\circ}\mathrm{C\,yr^{-1}}$ (solid orange arrow in Fig. 8). If all models used LWDR from CRUNCEP or WATCH, then applying the trend of annual LWDR (0.087 ± 0.023 $\mathrm{W\,m^{-2}\,yr^{-1}}$ from CRUNCEP and 0.187 ± 0.028 $\mathrm{W\,m^{-2}\,yr^{-1}}$ from WATCH) during the period 1960–2000 as an emerging observation constraint empirical relationship in Fig. 8, the posterior range is reduced compared with the prior $\dot{T}_s$ range (black curve in right panel of Fig. 8). Overall, the total uncertainty range of $\dot{T}_s$ at 20 cm ($\sim 0.02\,^{\circ}\mathrm{C\,yr^{-1}}$, defined as the spread of $\dot{T}_s$ at

TCD
9, 2301–2337, 2015

20 cm across the models) can be broken down into FU ($0.021 \pm 0.008\,^{\circ}\mathrm{C\,yr^{-1}}$) and SU ($0.012 \pm 0.001\,^{\circ}\mathrm{C\,yr^{-1}}$). Since FU and SU are not independent, the total uncertainty of $\dot{T}_s$ at 20 cm is not the sum of FU and SU.

Further, we found that correlation coefficients between trends of summer T_s at 20 cm and at 1 m and summer LWDR over boreal regions are statistically significant ($P < 0.05$) (Fig. S7). This is also found for winter (November to March) T_s at 20 cm and 1 m (Fig. S8). Trends of summer and winter T_s at 20 cm or 1 m are not significantly correlated with other climate drivers than LWDR (snowfall, rainfall, T_a and SWDR) across the models ($P > 0.05$).

Meteorological stations are sparse in the cold permafrost regions. For example, there are only 8.8 stations per million km^2 north of 60° N in the CRU TS3.22 gridded air temperature product compared to 41.1 stations per million km^2 between 25 and 60° N. This results in uncertainty in gridded climate products over Arctic regions, especially for trends of Arctic climate variables (Mitchell and Jones, 2005; Troy and Wood, 2009; Rawlins et al., 2010; Weedon et al., 2011). We found that the FU dominates the total uncertainty of $\dot{T}_s$. This suggests that modelers not only need to improve their models, but also need better climate forcing data (or need to test the effects of different climate input data) when modeling long term changes of T_s in permafrost regions. However, to quantify the SU, simulations using the same agreed upon climate forcing data are highly recommended to further attribute the contribution of each process in the soil thermal dynamics of models such as organic carbon insulation effects, snow insulation effects, latent heat formation and emission, soil conductivity and surface properties (see Lawrence and Slater, 2008; Koven et al., 2009; Bonfils et al., 2012; Gouttevin et al., 2012).

TCD
9, 2301–2337, 2015

3.5 Emerging constraint on how much near-surface permafrost has disappeared

All the nine models provide estimates of total boreal NSPA during 1960–2000 that ranges from 6.8 million km^2 in CoLM to 19.7 million km^2 in ORCHIDEE, which is three times as large as the former. The average of total NSPA in the nine models ensemble (12.5 million km^2) is smaller than the estimate from the International Permafrost Association (IPA) map (16.2 million km^2; Brown et al., 1998; Lawrence and Slater et al., 2013). A statistic model based on relationships between air temperature and permafrost shows that permafrost extent over Northern Hemisphere was also estimated in the range 12.9–17.8 million km^2 (Gruber, 2012), and six out of the nine models are within this range. Eight out of the nine models show a significant decrease in NSPA with climate warming during 1960–2000 (except UW-VIC). The loss rate of NSPA is found to vary by a factor of 13 across the nine models, varying from -4×10^3 $km^2\,yr^{-1}$ in MIROC-ESM to -50×10^3 $km^2\,yr^{-1}$ in JULES (Fig. 9a). The average of loss rate of NSPA across the models ($-23 \pm 23 \times 10^3$ $km^2\,yr^{-1}$) is smaller than in the previous estimations of Burke et al. (2013) and Slater and Lawrence (2013). For example, the loss rate of NSPA was estimated at -81×10^3–-55×10^3 $km^2\,yr^{-1}$ during the period 1967–2000 by JULES offline simulations with different climate forcing datasets (Burke et al., 2013). The ranges of loss rate of NSPA in BONA, BOEU and BOAS across the models are -16.6×10^3–2.2×10^3, -4.0×10^3–0.0×10^3 and -34.2×10^3–-1.1×10^3 $km^2\,yr^{-1}$, respectively (Fig. 9). This is consistent with the observed permafrost degradation (decrease in thickness) in these regions (Vaughan et al., 2013).

The retreat rate of NSPA is not correlated significantly with the initial NSPA of each model ($R = -0.30$, $P = 0.438$), implying that the initial state of models is less important than their response to climate change in determining NSPA loss rates. On the contrary to the small effect of initial NSPA, the trend of summer T_s at 1 m is found to be strongly correlated with NSPA loss rates across the models of the ensemble. Figure 9 shows that the trend of summer T_s at 1 m can explain 73 % of the differences in NSPA loss

TCD
9, 2301–2337, 2015

rates between models. The sensitivity of NSPA loss rate to summer $\dot{T}_s$ at 1 m is estimated to be -2.80 ± 0.67 million $km^2\,°C^{-1}$, based on the linear regression between the loss rate of NSPA and the trend of summer T_s at 1 m across the nine models (Fig. 9). For the BONA, BOEU and BOAS sub-regions, the sensitivities of NSPA loss rate to summer $\dot{T}_s$ at 1 m are -0.74 ± 0.10, -0.09 ± 0.03 and -1.74 ± 0.59 million $km^2\,°C^{-1}$, respectively (Fig. 9). The sensitivity of future total NSPA changes to T_a over Pan-Arctic regions was estimated to be -1.67 ± 0.7 million $km^2\,°C^{-1}$, ranging from 0.2 to 3.5 million $km^2\,°C^{-1}$ in CMIP5 model ensembles (Slater and Lawrence, 2013; Koven et al., 2013). The average of summer T_s trends at 1 m is only 70 % (43–100 %) of $\dot{T}_a$ in the nine models, so that the sensitivity of total NSPA to T_a over boreal regions in the nine models is about -2.00 ± 0.47 million $km^2\,°C^{-1}$, which is larger than that from CMIP5 model ensemble, but comparable within the uncertainties of each estimate (Slater and Lawrence, 2013). Six out of the nine models of this study were also used as land surface schemes of the coupled CMIP5 models, but possibly for different versions.

A mean positive trend of summer LWDR of 0.073 ± 0.030 and 0.210 ± 0.027 W $m^2\,yr^{-1}$ over boreal regions from 1960 to 2000 are derived from the CRUNCEP and WATCH datasets respectively described in Sect. 2. We applied this trend of LWDR to an emerging constraint on summer T_s trends from the relationship between the trend of summer LWDR and the trend of summer T_s at 1 m (Fig. S7). This approach constrains the trend of summer T_s to $0.014 \pm 0.004\,°C\,yr^{-1}$ with CRUNCEP and to $0.027 \pm 0.004\,°C\,yr^{-1}$ with WATCH. The uncertainty is reduced by 50 % from the prior range including different models and different forcings. A total NSPA loss rate of $39 \pm 14 \times 10^3$ $km^2\,yr^{-1}$ can be constrained by multiplying the sensitivity of total NSPA loss rate to summer $\dot{T}_s$ at 1 m (-2.80 ± 0.67 million $km^2\,°C^{-1}$) by the trend of T_s at 1 m itself empirically estimated by $\dot{LWDR}$ during 1960–2000 from CRUNCEP ($0.014 \pm 0.004\,°C\,yr^{-1}$). The constrained loss rate of NSPA over BONA, BOEU and BOAS based upon the CRUNCEP $\dot{LWDR}$ from 1960 to 2000 are $11 \pm 5 \times 10^3$, $1 \pm 1 \times 10^3$ and $25 \pm 11 \times 10^3$ $km^2\,yr^{-1}$, respectively. Similarly, if WATCH $\dot{LWDR}$ is used to constrain NSPA loss rate, the total NSPA loss

TCD
9, 2301–2337, 2015

rate is $75 \pm 14 \times 10^3$ km^2 yr^{-1}, and loss rate of NSPA over BONA, BOEU and BOAS are estimated to be $28 \pm 10 \times 10^3$, $2 \pm 1 \times 10^3$ and $39 \pm 19 \times 10^3$ km^2 yr^{-1}, respectively. The southern boundary of the discontinuous permafrost zone shift northward during the past decades is also observed (Vaughan et al., 2013). The larger warming rate and higher sensitivity of NSPA loss to T_s over BOAS could explain the reason for significant degradation of permafrost over BOAS (Vaughan et al., 2013). The larger permafrost degradation rate in BOAS than that in BONA may have larger effects on changes in vegetation distribution and growth, and permafrost carbon in these two regions, and can be quantified in future studies. Obviously, there is a large difference in constrained NSPA between CRUNCEP and WATCH. In the future, long-term climate reanalysis including radiation evaluated against sites with long-term radiation measurements (http://www.geba.ethz.ch) would be extremely useful for land surface models to provide improved estimate of NSPA.

4 Conclusions

In this study, trends of T_s over boreal regions from nine process-based models were analyzed for the past 40 years. All models produce a warming of T_s, but the trends of T_s at 20 cm depth range from 0.010 ± 0.003 °C yr^{-1} (CoLM) to 0.031 ± 0.005 °C yr^{-1} (UVic) during 1960–2000. Most models show a smaller increase of T_s with deeper depth. T_a and LWDR are found to be the predominant drivers of the increase in T_s averaged across large spatial scales. The relative contribution of T_a and LWDR trends to the increase of T_s is however different across the models. The total uncertainty of the trend of T_s at 20 cm is decomposed into the uncertainty contributed by uncertain climate forcing datasets (0.021 ± 0.008 °C yr^{-1}) and the uncertainty reflecting model structure (0.012 ± 0.001 °C yr^{-1}). The NSPA loss rate is significantly correlated among the model results with the simulated trend of T_s at 1 m, with a linear sensitivity of total NSPA loss rate to summer $\dot{T}_s$ at 1 m of -2.80 ± 0.67 million km^2 °C^{-1}. Based on LWDR from

TCD
9, 2301–2337, 2015

CRUNCEP and WATCH data, the total NSPA decrease is estimated to be $39 \pm 14 \times 10^3$–$75 \pm 14 \times 10^3$ km^2 yr^{-1} from 1960 to 2000. The constraint method used in this study could be applied to estimate historical and future permafrost degradation rate, and further to quantify the permafrost carbon loss by permafrost carbon distribution map.

Given that meteorological stations are sparse in the cold permafrost regions, especially in Siberia and other unpopulated land in the north, the gridded climate products over high-latitude regions have a large uncertainty as well (Mitchell and Jones, 2005; Rawlins et al., 2010; Weedon et al., 2011). This large uncertainty could propagate into simulated permafrost dynamics and feedbacks. More sites are needed in high-latitude regions for reducing the climate uncertainty. Since the beginning of the satellite era, microwave emissivity data related to land surface temperature has become increasingly available (e.g. Smith et al., 2004). These images could be used to independently evaluate soil surface temperature in models on a large scale, although they have their own uncertainties. In addition, many complex processes affect permafrost thermal dynamics in the models, such as soil organic insulation effects, snow insulation effects, soil freeze–thaw etc., it is valuable to evaluate the uncertainty of each process effects on soil thermal dynamics simulations based on site measurements. This could be helpful for reducing permafrost simulation uncertainty.

The Supplement related to this article is available online at doi:10.5194/tcd-9-2301-2015-supplement.

Acknowledgements. This study has been supported by the PAGE21 project, funded by the European Commission FP7-ENV-2011 (grant agreement NO. 282700) and has been developed as part of the modeling integration team of the Permafrost Carbon Network (PCN, www.permafrostcarbon.org) funded by the National Science Foundation. Any use of trade, firm, or product names is for descriptive purposes only and does not imply endorsement by the US Government.

TCD
9, 2301–2337, 2015

References

Adam, J. C., Clark, E. A., Lettenmaier, D. P., and Wood, E. F.: Correction of global precipitation products for orographic effects, J. Climate, 19, 15–38, doi:10.1175/jcli3604.1, 2006.

Alexeev, V. A., Nicolsky, D. J., Romanovsky, V. E., and Lawrence, D. M.: An evaluation of deep soil configurations in the CLM3 for improved representation of permafrost, Geophys. Res. Lett., 34, L09502, doi:10.1029/2007gl029536, 2007.

Avis, C. A., Weaver, A. J., and Meissner, K. J.: Reduction in areal extent of high-latitude wetlands in response to permafrost thaw, Nat. Geosci., 4, 444–448, 2011.

Best, M. J., Pryor, M., Clark, D. B., Rooney, G. G., Essery, R.L. H., Ménard, C. B., Edwards, J. M., Hendry, M. A., Porson, A., Gedney, N., Mercado, L. M., Sitch, S., Blyth, E., Boucher, O., Cox, P. M., Grimmond, C. S. B., and Harding, R. J.: The Joint UK Land Environment Simulator (JULES), model description – Part 1: Energy and water fluxes, Geosci. Model Dev., 4, 677–699, doi:10.5194/gmd-4-677-2011, 2011.

Bohn, T. J., Podest, E., Schroeder, R., Pinto, N., McDonald, K. C., Glagolev, M., Filippov, I., Maksyutov, S., Heimann, M., Chen, X., and Lettenmaier, D. P.: Modeling the large-scale effects of surface moisture heterogeneity on wetland carbon fluxes in the West Siberian Lowland, Biogeosciences, 10, 6559–6576, doi:10.5194/bg-10-6559-2013, 2013.

Bonfils, C. J. W., Phillips, T. J., Lawrence, D. M., Cameron-Smith, P., Riley, W. J., and Subin, Z. M.: On the influence of shrub height and expansion on northern high latitude climate, Environ. Res. Lett., 7, 015503, doi:10.1088/1748-9326/7/1/015503, 2012.

Brown, J., Ferrians Jr., O. J., Heginbottom, J. A., and Melnikov, E. S.: Circum-Arctic map of permafrost and ground-ice conditions, Digital Media, National Snow and Ice Data Center/World Data Center for Glaciology, Boulder, CO, 1998, revised February 2001.

Burke, E., Dankers, R., Jones, C., and Wiltshire, A.: A retrospective analysis of pan Arctic permafrost using the JULES land surface model, Clim. Dynam., 41, 1025–1038, doi:10.1007/s00382-012-1648-x, 2013.

Clark, D. B., Mercado, L. M., Sitch, S., Jones, C. D., Gedney, N., Best, M. J., Pryor, M., Rooney, G. G., Essery, R. L. H., Blyth, E., Boucher, O., Harding, R. J., Huntingford, C., and Cox, P. M.: The Joint UK Land Environment Simulator (JULES), model description – Part 2: Carbon fluxes and vegetation dynamics, Geosci. Model Dev., 4, 701–722, doi:10.5194/gmd-4-701-2011, 2011.

TCD
9, 2301–2337, 2015

Dai, Y., Zeng, X., Dickinson, R. E., Baker, I., Bonan, G. B., Bosilovich, M. G., Denning, A. S., Dirmeyer, P. A., Houser, P. R., Niu, G., Oleson, K. W., Schlosser, C. A., and Yang, Z.-L.: The Common Land Model, B. Am. Meteorol. Soc., 84, 1013–1023, doi:10.1175/bams-84-8-1013, 2003.

Dai, Y., Dickinson, R. E., and Wang, Y.-P.: A two-big-leaf model for canopy temperature, photosynthesis, and stomatal conductance, J. Climate, 17, 2281–2299, doi:10.1175/1520-0442(2004)017<2281:atmfct>2.0.co;2, 2004.

Decharme, B., Boone, A., Delire, C., and Noilhan, J.: Local evaluation of the interaction between soil biosphere atmosphere soil multilayer diffusion scheme using four pedotransfer functions, J. Geophys. Res.-Atmos., 116, D20126, doi:10.1029/2011jd016002, 2011.

Decharme, B., Martin, E., and Faroux, S.: Reconciling soil thermal and hydrological lower boundary conditions in land surface models, J. Geophys. Res.-Atmos., 118, 7819–7834, doi:10.1002/jgrd.50631, 2013.

Elberling, B., Michelsen, A., Schadel, C., Schuur, E. A. G., Christiansen, H. H., Berg, L., Tamstorf, M. P., and Sigsgaard, C.: Long-term CO_2 production following permafrost thaw, Nature Clim. Change, 3, 890–894, doi:10.1038/nclimate1955, 2013.

Field, C. B., Jackson, R. B., and Mooney, H. A.: Stomatal responses to increased CO_2: implications from the plant to the global scale, Plant Cell Environ., 18, 1214–1225, doi:10.1111/j.1365-3040.1995.tb00630.x, 1995.

Gouttevin, I., Krinner, G., Ciais, P., Polcher, J., and Legout, C.: Multi-scale validation of a new soil freezing scheme for a land-surface model with physically-based hydrology, The Cryosphere, 6, 407–430, doi:10.5194/tc-6-407-2012, 2012.

Gruber, S.: Derivation and analysis of a high-resolution estimate of global permafrost zonation, The Cryosphere, 6, 221–233, doi:10.5194/tc-6-221-2012, 2012.

Harris, I., Jones, P. D., Osborn, T. J., and Lister, D. H.: Updated high-resolution grids of monthly climatic observations – the CRU TS3.10 Dataset, Int. J. Climatol., 34, 623–642, doi:10.1002/joc.3711, 2014.

Hugelius, G., Strauss, J., Zubrzycki, S., Harden, J. W., Schuur, E. A. G., Ping, C.-L., Schirrmeister, L., Grosse, G., Michaelson, G. J., Koven, C. D., O'Donnell, J. A., Elberling, B., Mishra, U., Camill, P., Yu, Z., Palmtag, J., and Kuhry, P.: Estimated stocks of circumpolar permafrost carbon with quantified uncertainty ranges and identified data gaps, Biogeosciences, 11, 6573–6593, doi:10.5194/bg-11-6573-2014, 2014.

TCD
9, 2301–2337, 2015

Kalnay, E., Kanamitsu, M., Kistler, R., Collins, W., Deaven, D., Gandin, L., Iredell, M., Saha, S., White, G., Woollen, J., Zhu, Y., Leetmaa, A., Reynolds, R., Chelliah, M., Ebisuzaki, W., Higgins, W., Janowiak, J., Mo, K. C., Ropelewski, C., Wang, J., Jenne, R., and Joseph, D.: The NCEP/NCAR 40-Year Reanalysis Project, B. Am. Meteorol. Soc., 77, 437–471, doi:10.1175/1520-0477(1996)077<0437:tnyrp>2.0.co;2, 1996.

Khvorostyanov, D. V., Ciais, P., Krinner, G., Zimov, S. A., Corradi, C., and Guggenberger, G.: Vulnerability of permafrost carbon to global warming. Part II: Sensitivity of permafrost carbon stock to global warming, Tellus B, 60, 265–275, doi:10.1111/j.1600-0889.2007.00336.x, 2008.

Koven, C., Friedlingstein, P., Ciais, P., Khvorostyanov, D., Krinner, G., and Tarnocai, C.: On the formation of high-latitude soil carbon stocks: effects of cryoturbation and insulation by organic matter in a land surface model, Geophys. Res. Lett., 36, L21501, doi:10.1029/2009gl040150, 2009.

Koven, C. D., Ringeval, B., Friedlingstein, P., Ciais, P., Cadule, P., Khvorostyanov, D., Krinner, G., and Tarnocai, C.: Permafrost carbon-climate feedbacks accelerate global warming, P. Natl. Acad. Sci. USA, 108, 14769–14774, doi:10.1073/pnas.1103910108, 2011.

Koven, C. D., Riley, W. J., and Stern, A.: Analysis of permafrost thermal dynamics and response to climate change in the CMIP5 Earth System Models, J. Climate, 26, 1877–1900, doi:10.1175/jcli-d-12-00228.1, 2013.

Krinner, G., Viovy, N., de Noblet-Ducoudré, N., Ogée, J., Polcher, J., Friedlingstein, P., Ciais, P., Sitch, S., and Prentice, I. C.: A dynamic global vegetation model for studies of the coupled atmosphere–biosphere system, Global Biogeochem. Cy., 19, GB1015, doi:10.1029/2003gb002199, 2005

Lawrence, D. and Slater, A.: Incorporating organic soil into a global climate model, Clim. Dynam., 30, 145–160, doi:10.1007/s00382-007-0278-1, 2008.

Lawrence, D. M., Slater, A. G., Romanovsky, V. E., and Nicolsky, D. J.: Sensitivity of a model projection of near-surface permafrost degradation to soil column depth and representation of soil organic matter, J. Geophys. Res.-Earth, 113, F02011, doi:10.1029/2007jf000883, 2008.

MacDougall, A. H., Avis, C. A., and Weaver, A. J.: Significant contribution to climate warming from the permafrost carbon feedback, Nat. Geosci., 5, 719–721„ 2012.

McGuire, A. D., Anderson, L. G., Christensen, T. R., Dallimore, S., Guo, L., Hayes, D. J., Heimann, M., Lorenson, T. D., Macdonald, R. W., and Roulet, N.: Sensitivity of the carbon

TCD
9, 2301–2337, 2015

cycle in the Arctic to climate change, Ecol. Monogr., 79, 523–555, doi:10.1890/08-2025.1, 2009.
McGuire, A. D., Christensen, T. R., Hayes, D., Heroult, A., Euskirchen, E., Kimball, J. S., Koven, C., Lafleur, P., Miller, P. A., Oechel, W., Peylin, P., Williams, M., and Yi, Y.: An assessment of the carbon balance of Arctic tundra: comparisons among observations, process models, and atmospheric inversions, Biogeosciences, 9, 3185–3204, doi:10.5194/bg-9-3185-2012, 2012.
McGuire, D. Lawrence, D., Burke, E., Chen, X., Delire, C., Koven, C., MacDougall, A., Peng, S., Rinke, A., Saito, K., Zhang, W., Alkama, R., J. Bohn, T., Ciais, P., Decharme, B., Gouttevin, I., Hajima, T., Ji, D., Krinner, G., Lettenmaier, D. P., Miller, P., Moore, J. C., Smith, B., and Sueyoshiet, T.: An retrospective assessment of the vulnerability of permafrost carbon in the earth system: comparison of dynamics among process-based models, in preparation, 2015.
Mitchell, T. D. and Jones, P. D.: An improved method of constructing a database of monthly climate observations and associated high-resolution grids, Int. J. Climatol., 25, 693–712, doi:10.1002/joc.1181, 2005.
Oleson, K. W., Lawrence, D. M., Bonan, G. B., Drewniak, B., Huang, M., Koven, C. D., Levis, S., Li, F., Riley, W. J., Subin, Z. M., Swenson, S. C., Thornton, P. E., Bozbiyik, A., Fisher, R., Heald, C. L., Kluzek, E., Lamarque, J., Lawrence, P. J., Leung, L. R., Lipscomb, W., Muszala, S., Ricciuto, D. M., Sacks, W., Tang, J., and Yang, Z.: Technical Description of Version 4.5 of the Community Land Model (CLM), NCAR Technical Note #NCAR/TN-503+STR, National Center for Atmospheric Research, P.O. Box 3000 Boulder, Colorado 80307-3000, 2013.
Osterkamp, T. E.: A thermal history of permafrost in Alaska, in: Proceedings of Eighth International Conference on Permafrost, Zurich, 863–868, The 8th International Conference on Permafrost in Zürich, Switzerland, 21–25 July, 2003.
Osterkamp, T. E.: Characteristics of the recent warming of permafrost in Alaska, J. Geophys. Res.-Earth, 112, F02S02, doi:10.1029/2006jf000578, 2007.
Park, H., Sherstiukov. A. B., Fedorov, A. N., Polyakov, I. V., and Walsh, J. E.: An observation-based assessment of the influences of air temperature and snow depth on soil temperature in Russia, Environ. Res. Lett., 9, 064026, doi:10.1088/1748-9326/9/6/064026, 2014.
Qian, B., Gregorich, E. G., Gameda, S., Hopkins, D. W., and Wang, X. L.: Observed soil temperature trends associated with climate change in Canada, J. Geophys. Res.-Atmos., 116, D02106, doi:10.1029/2010jd015012, 2011.

TCD
9, 2301–2337, 2015

Rawlins, M. A., Steele, M., Holland, M. M., Adam, J. C., Cherry, J. E., Francis, J. A., Groisman, P. Y., Hinzman, L. D., Huntington, T. G., Kane, D. L., Kimball, J. S., Kwok, R., Lammers, R. B., Lee, C. M., Lettenmaier, D. P., McDonald, K. C., Podest, E., Pundsack, J. W., Rudels, B., Serreze, M. C., Shiklomanov, A., Skagseth, O., Troy, T. J., Vorosmarty, C. J., Wensnahan, M., Wood, E. F., Woodgate, R., Yang, D. Q., Zhang, K., and Zhang, T. J.: Analysis of the Arctic system for freshwater cycle intensification: observations and expectations, J. Climate, 23, 5715–5737, doi:10.1175/2010jcli3421.1, 2010.

Rawlins, M. A., McGuire, A. D., Kimball, J. K., Dass, P., Lawrence, D., Burke, E., Chen, X., Delire, C., Koven, C., MacDougall, A., Peng, S., Rinke, A., Saito, K., Zhang, W., Alkama, R., J. Bohn, T., Ciais, P., Decharme, B., Gouttevin, I., Hajima, T., Ji, D., Krinner, G., Lettenmaier, D. P., Miller, P., Moore, J. C., Smith, B., and Sueyoshi, T.: Assessment of model estimates of land–atmosphere CO_2 exchange across Northern Eurasia, Biogeosciences Discuss., 12, 2257–2305, doi:10.5194/bgd-12-2257-2015, 2015.

Romanovsky, V. E., Sazonova, T. S., Balobaev, V. T., Shender, N. I., and Sergueev, D. O.: Past and recent changes in air and permafrost temperatures in eastern Siberia, Global Planet. Change, 56, 399–413, doi:10.1016/j.gloplacha.2006.07.022, 2007.

Romanovsky, V. E., Smith, S. L., and Christiansen, H. H.: Permafrost thermal state in the polar Northern Hemisphere during the international polar year 2007–2009: a synthesis, Permafrost Periglac., 21, 106–116, 2010.

Schädel, C., Schuur, E. A. G., Bracho, R., Elberling, B., Knoblauch, C., Lee, H., Luo, Y., Shaver, G. R., and Turetsky, M. R.: Circumpolar assessment of permafrost C quality and its vulnerability over time using long-term incubation data, Glob. Change Biol., 20, 641–652, doi:10.1111/gcb.12417, 2014.

Schaefer, K., Zhang, T., Bruhwiler, L., and Barrett, A. P.: Amount and timing of permafrost carbon release in response to climate warming, Tellus B, 63, 165–180, doi:10.1111/j.1600-0889.2011.00527.x, 2011.

Schneider von Deimling, T., Meinshausen, M., Levermann, A., Huber, V., Frieler, K., Lawrence, D. M., and Brovkin, V.: Estimating the near-surface permafrost-carbon feedback on global warming, Biogeosciences, 9, 649–665, doi:10.5194/bg-9-649-2012, 2012.

Schuur, E. A. G., Bockheim, J., Canadell, J. G., Euskirchen, E., Field, C. B., Goryachkin, S. V., Hagemann, S., Kuhry, P., Lafleur, P. M., Lee, H., Mazhitova, G., Nelson, F. E., Rinke, A., Romanovsky, V. E., Shiklomanov, N., Tarnocai, C., Venevsky, S., Vogel, J. G., and Zimov, S. A.:

TCD
9, 2301–2337, 2015

Vulnerability of permafrost carbon to climate change: implications for the global carbon cycle, BioScience, 58, 701–714, doi:10.1641/b580807, 2008.
Sheffield, J., Goteti, G., and Wood, E. F.: Development of a 50-year high-resolution global dataset of meteorological forcings for land surface modeling, J. Climate, 19, 3088–3111, doi:10.1175/jcli3790.1, 2006.
Slater, A. G. and Lawrence, D. M.: Diagnosing present and future permafrost from climate models, J. Climate, 26, 5608–5623, doi:10.1175/jcli-d-12-00341.1, 2013.
Smith, B., Prentice, I. C., and Sykes, M. T.: Representation of vegetation dynamics in the modelling of terrestrial ecosystems: comparing two contrasting approaches within European climate space, Global Ecol. Biogeogr., 10, 621–637, doi:10.1046/j.1466-822X.2001.t01-1-00256.x, 2001.
Smith, N. V., Saatchi, S. S., and Randerson, J. T.: Trends in high northern latitude soil freeze and thaw cycles from 1988 to 2002, J. Geophys. Res.-Atmos., 109, D12101, doi:10.1029/2003JD004472, 2004.
Smith, S. L., Burgess, M. M., Riseborough, D., and Mark Nixon, F.: Recent trends from Canadian permafrost thermal monitoring network sites, Permafrost Periglac., 16, 19–30, 2005.
Smith, S. L., Romanovsky, V. E., Lewkowicz, A. G., Burn, C. R., Allard, M., Clow, G. D., Yoshikawa, K., and Throop, J.: Thermal state of permafrost in North America: a contribution to the international polar year, Permafrost Periglac., 21, 117–135, 2010.
Smith, S. L., Throop, J., and Lewkowicz, A. G.: Recent changes in climate and permafrost temperatures at forested and polar desert sites in northern Canada, Can. J. Earth Sci., 49, 914–924, doi:10.1139/e2012-019, 2012.
Stevens, M. B., Smerdon, J. E., González-Rouco, J. F., Stieglitz, M., and Beltrami, H.: Effects of bottom boundary placement on subsurface heat storage: implications for climate model simulations, Geophys. Res. Lett., 34, L02702, doi:10.1029/2006gl028546, 2007.
Troy, T. J. and Wood, E. F.: Comparison and evaluation of gridded radiation products across northern Eurasia, Environ. Res. Lett., 4, 045008, doi:10.1088/1748-9326/4/4/045008, 2009.
Vaughan, D. G., Comiso, J. C., Allison, I., Carrasco, J., Kaser, G., Kwok, R., Mote, P., Murray, T., Paul, F., Ren, J., Rignot, E., Solomina, O., Steffen, K., and Zhang, T.: Observations: Cryosphere, in: Climate Change 2013: The Physical Science Basis. Contribution of Working Group I to the Fifth Assessment Report of the Intergovernmental Panel on Climate Change, edited by: Stocker, T. F., Qin, D., Plattner, G.-K., Tignor, M., Allen, S. K., Boschung, J.,

TCD
9, 2301–2337, 2015

Nauels, A., Xia, Y., Bex, V. and Midgley, P. M., Cambridge University Press, Cambridge, UK and New York, NY, USA, 317–382, doi:10.1017/CBO9781107415324.012, 2013.
Watanabe, S., Hajima, T., Sudo, K., Nagashima, T., Takemura, T., Okajima, H., Nozawa, T., Kawase, H., Abe, M., Yokohata, T., Ise, T., Sato, H., Kato, E., Takata, K., Emori, S., and Kawamiya, M.: MIROC-ESM 2010: model description and basic results of CMIP5-20c3m experiments, Geosci. Model Dev., 4, 845–872, doi:10.5194/gmd-4-845-2011, 2011.
Weedon, G. P., Gomes, S., Viterbo, P., Shuttleworth, W. J., Blyth, E., Österle, H., Adam, J. C., Bellouin, N., Boucher, O., and Best, M.: Creation of the WATCH Forcing Data and its use to assess global and regional reference crop evaporation over land during the twentieth century, J. Hydrometeorol., 12, 823–848, doi:10.1175/2011jhm1369.1, 2011.
Weedon, G. P., Balsamo, G., Bellouin, N., Gomes, S., Best, M. J., and Viterbo, P.: The WFDEI meteorological forcing data set: WATCH Forcing Data methodology applied to ERA-Interim reanalysis data, Water Resour. Res., 50, 7505–7514, doi:10.1002/2014wr015638, 2014.
Wei, Y., Liu, S., Huntzinger, D. N., Michalak, A. M., Viovy, N., Post, W. M., Schwalm, C. R., Schaefer, K., Jacobson, A. R., Lu, C., Tian, H., Ricciuto, D. M., Cook, R. B., Mao, J., and Shi, X.: The North American Carbon Program Multi-scale Synthesis and Terrestrial Model Intercomparison Project – Part 2: Environmental driver data, Geosci. Model Dev., 7, 2875–2893, doi:10.5194/gmd-7-2875-2014, 2014.
Willmott, C. J. and Matsuura, K.: Terrestrial Air Temperature and Precipitation: Monthly and Annual Time Series (1950–1999), available at: http://climate.geog.udel.edu/~climate/html_pages/README.ghcn_ts2.html (last access: 2 February 2015), 2001.
Zhang, T., Barry, R., Gilichinsky, D., Bykhovets, S. S., Sorokovikov, V. A., and Ye, J.: An amplified signal of climatic change in soil temperatures during the last century at Irkutsk, Russia, Climatic Change, 49, 41–76, doi:10.1023/a:1010790203146, 2001.

TCD
9, 2301–2337, 2015

Table 1. Soil depth for soil thermal dynamics and climate forcing used in each model.

Model	Soil depth (m)	Climate forcing (Reference)	Model reference	Note
CLM	45.1	CRUNCEP v4 (http://dods.extra.cea.fr/)	Oleson et al. (2013)	–
CoLM	3.4	Princeton (Sheffield et al., 2006)	Dai et al. (2003, 2004)	
ISBA	12.0	WATCH (1901–2010) (Weedon et al., 2011)	Decharme et al. (2011, 2013)	–
JULES	20.8	WATCH (1901–2001) (Weedon et al., 2011)	Best et al. (2011), Clark et al. (2011)	
LPJ-GUESS	3.0	CRU TS 3.1 (Harris et al., 2014)	Smith et al. (2001), McGuire et al. (2012)	Surface shortwave downward radiation was calculated from cloudiness data set; no longwave downward radiation and vapor pressure were used.
MIROC-ESM	14.0	CMIP5 Drivers (Watanabe et al., 2011)	Watanabe et al. (2011)	
ORCHIDEE	47.4	WATCH (1901–1978) WFDEI (1978–2009) (Weedon et al., 2011, 2014)	Krinner et al. (2005), Koven et al. (2011), Gouttevin et al. (2012)	
UVic	250.3	CRUNCEP v4 (http://dods.extra.cea.fr/)	Avis et al. (2011), MacDougall et al. (2012)	Surface shortwave and longwave downward radiation were internally calculated.
UW-VIC	25.0	temperature from CRU TS3.1, precipitation from UDel, wind speed from NCEP-NCAR (Mitchell and Jones, 2005; Willmott and Matsura, 2001; Adam et al., 2006; Kalnay et al., 1996)	Bohn et al. (2013)	Surface shortwave and longwave downward radiation were internally calculated.

TCD
9, 2301–2337, 2015

Table 2. Description of simulations used in this study.

Simulation ID	Climate	CO_2
R01	variable	variable
R02	variable, but with detrended T_a	variable
R03	variable	constant in the year of 1960
R04	variable, but with detrended T_a and precipitation	variable
R05	variable, but with detrended T_a and LWDR	variable
R06	variable, but with detrended T_a, precipitation and LWDR	variable

TCD
9, 2301–2337, 2015

Table 3. The trends of annual air temperature (T_a), precipitation and longwave downward radiation (LWDR) in the second to fourth columns. The fifth column shows the trends of annual T_s at 20 cm in the reference simulation (R01). The last four columns show the contributions of drivers (T_a, precipitation, CO_2 and LWDR) on the trend of T_s as mentioned in Methods section. The relative contributions (divided by the trend of T_s in Ref) are shown in the parentheses. The bold font indicates statistically significant ($P < 0.05$).

Model	Trend of T_a (°C yr^{-1})	Trend of precipitation (mm yr^{-2})	Trend of LWDR (W m^{-2} yr^{-1})	Simulated Trend of T_s (R01) (°C yr^{-1})	Contribution from T_a (R01–R02) (°C yr^{-1})	Contribution from precipitation (R02–R04) (°C yr^{-1})	Contribution from CO_2 (R01–R03) (°C yr^{-1})	Contribution from LWDR (R02–R05) (°C yr^{-1})
CLM	**0.031**	0.13	**0.114**	**0.016 (100 %)**	**0.015 (92 %)**	**−0.002 (− 12 %)**	**0.001 (4 %)**	–
CoLM	**0.031**	−0.05	**0.058**	**0.010 (100 %)**	–	–	–	–
ISBA	**0.033**	−0.17	**0.183**	**0.030 (100 %)**	**0.030 (99 %)**	**0.001 (2 %)**	**0.000 (− 1 %)**	–
JULES	**0.034**	**0.31**	**0.189**	**0.017 (100 %)**	**−0.001 (− 6 %)**	−0.005 (−28 %)	**0.000 (0 %)**	**0.005 (31 %)**
LPJ-GUESS	**0.033**	0.11		**0.026 (100 %)**	**0.018 (67 %)**	0.000 (−1 %)	**−0.001 (− 5 %)**	–
MIROC-ESM	**0.025**	0.44	**0.140**	**0.024 (100 %)**	–	–	–	–
ORCHIDEE	**0.045**	0.00	**0.201**	**0.030 (100 %)**	**0.010 (34 %)**	**0.002 (7 %)**	**0.001 (2 %)**	**0.017 (56 %)**
UVic	**0.031**	0.11		**0.031 (100 %)**	**0.017 (56 %)**	**0.000 (0 %)**	0.000 (−1 %)	–
UW-VIC	**0.031**	**2.01**	**0.125**	**0.011 (100 %)**	**0.029 (266 %)**	−0.005 (−47 %)	**0.000 (0 %)**	–

TCD
9, 2301–2337, 2015

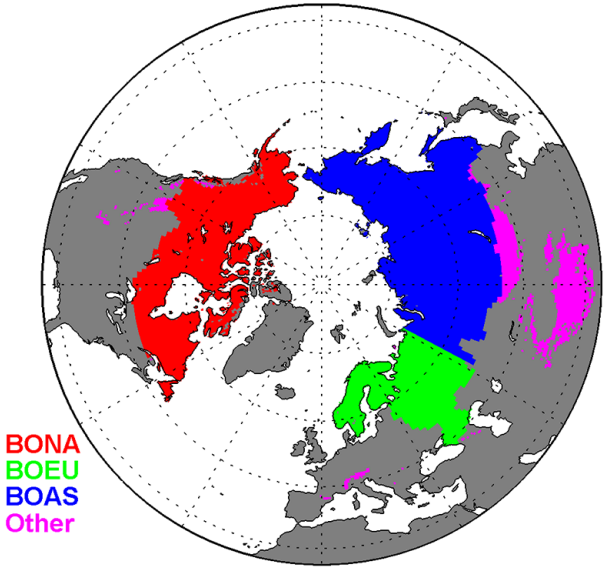

Figure 1. The spatial extent of regions defined in this study. Red, green, blue and magenta indicate the regions of boreal North America (BONA), boreal Europe (BOEU) and boreal Asia (BOAS), other permafrost areas (Other), respectively. We only selected BONA, BOEU and BOAS sub-regions for analysis in this study.

TCD
9, 2301–2337, 2015

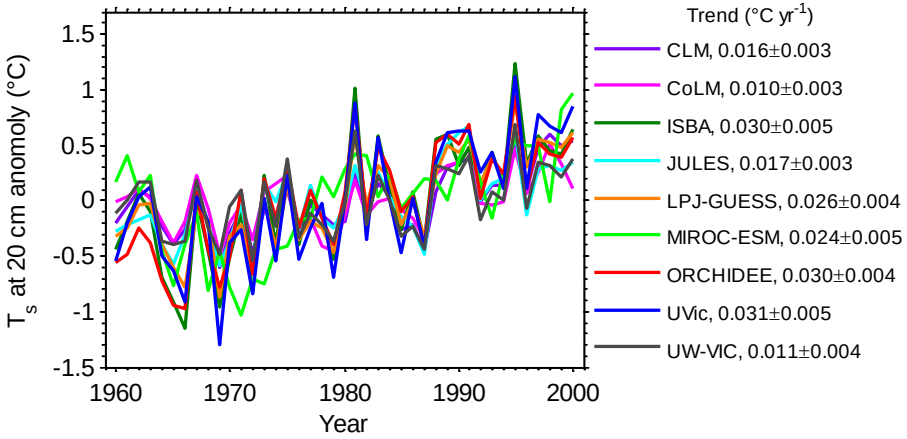

Figure 2. Simulated anomaly of annual T_s at 20 cm averaged over boreal regions of each model, during the period of 1960–2000.

TCD
9, 2301–2337, 2015

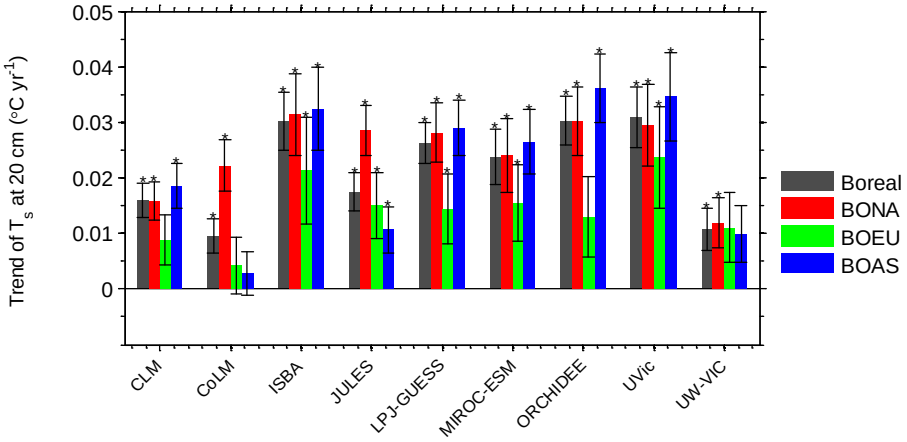

Figure 3. Simulated trends of annual T_s at 20 cm averaged over boreal regions and sub-regions of each model, from 1960 to 2000. * indicates significant trend of T_s ($P < 0.05$).

TCD
9, 2301–2337, 2015

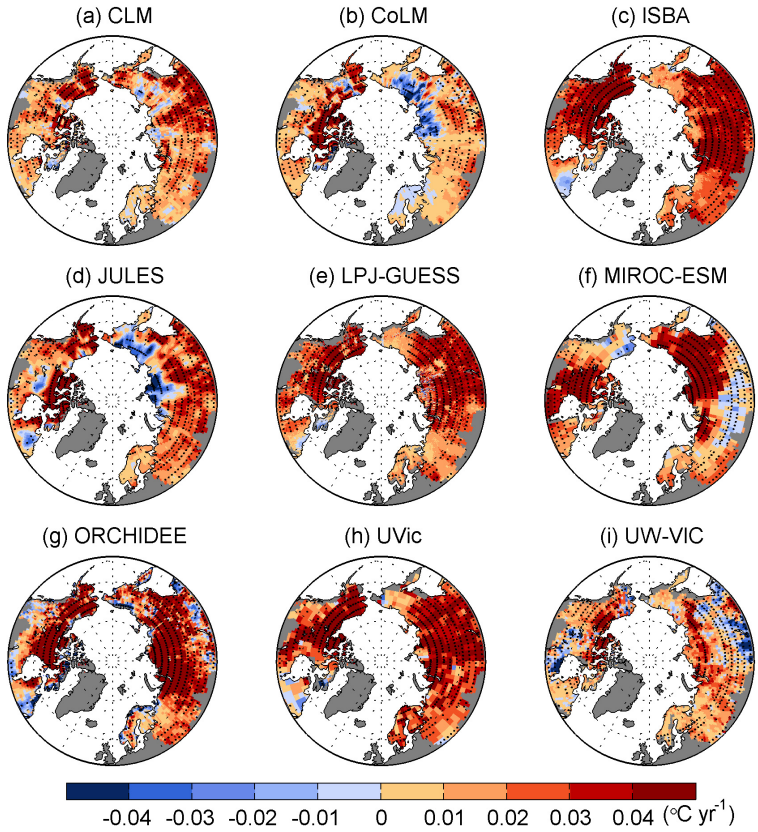

Figure 4. Spatial distributions of trends of annual T_s at 20 cm over boreal regions from 1960 to 2000 in **(a)** CLM, **(b)** CoLM, **(c)** ISBA, **(d)** JULES, **(e)** LPJ-GUESS, **(f)** MICRO-ESM, **(g)** ORCHIDEE, **(h)** UVic and **(i)** UW-VIC models. The black dots indicate regions with significant trends of T_s ($P < 0.05$).

TCD
9, 2301–2337, 2015

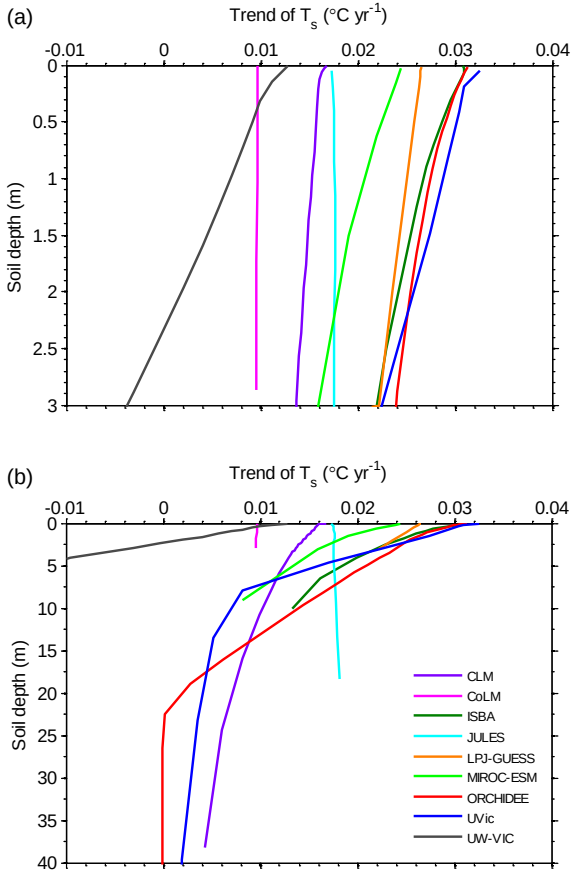

Figure 5. Simulated trends of annual T_s over boreal regions as a function of soil depths **(a)** 0–3 m and **(b)** 0–40 m for the nine models. Note the different total soil depths of the models.

TCD
9, 2301–2337, 2015

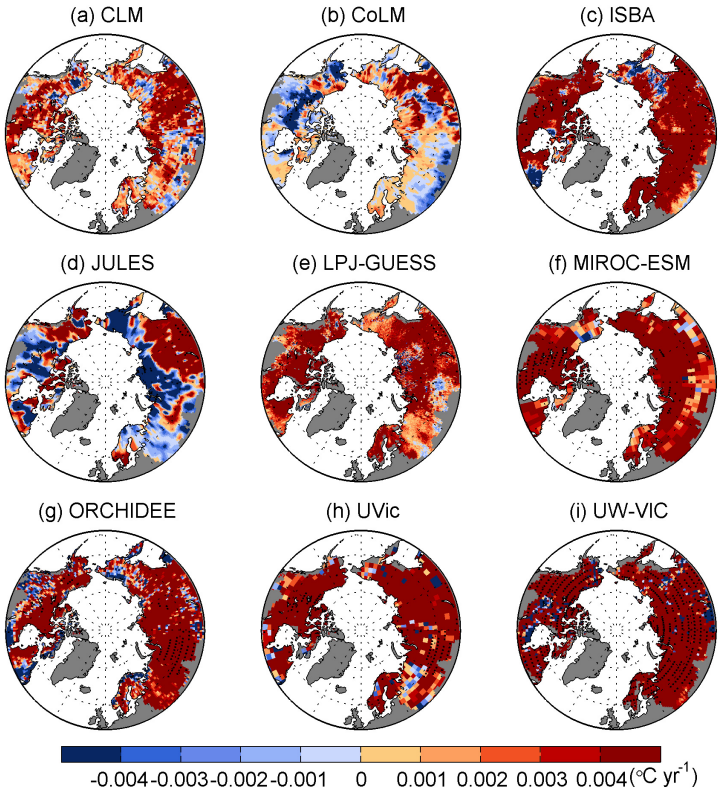

Figure 6. Spatial distributions of difference in trends of annual T_s at 0.2 and 3 m over boreal regions from 1960 to 2000 in **(a)** CLM, **(b)** CoLM, **(c)** ISBA, **(d)** JULES, **(e)** LPJ-GUESS, **(f)** MICRO-ESM, **(g)** ORCHIDEE, **(h)** UVic and **(i)** UW-VIC models. The black dots indicate statistically significant difference by t test ($P < 0.05$).

TCD
9, 2301–2337, 2015

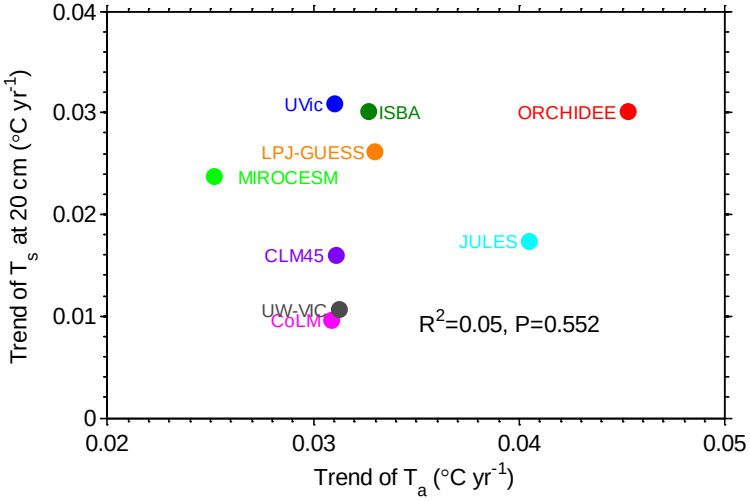

Figure 7. Simulated trends of annual T_s at 20 cm and T_a in the climate forcing data across the nine models.

TCD
9, 2301–2337, 2015

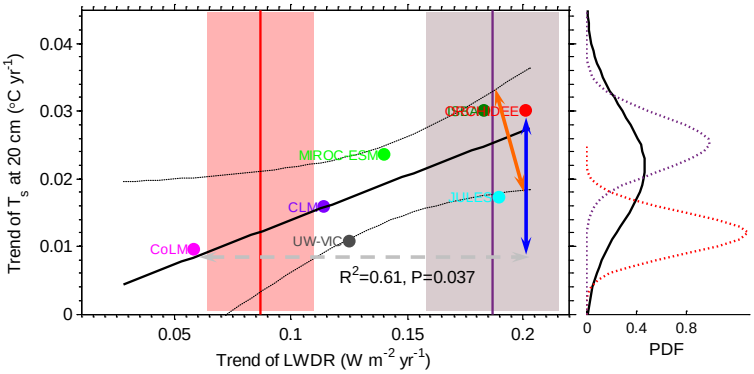

Figure 8. Simulated trends of annual T_s at 20 cm and annual LWDR in the climate forcing data over boreal regions across the seven models which used and provided LWDR in their climate forcing. The black dotted lines indicate the linear regression and 95 % confidence interval. The gray dashed line indicates the uncertainty of trend of LWDR in the climate forcing data. The solid blue and orange lines with double arrows indicate FU and SU, respectively. The red solid line with shade area shows the trend of LWDR ($0.087 \pm 0.023\,\mathrm{W\,m^{-2}\,yr^{-1}}$) during the period 1960–2000 from CRUNCEP v5.2 dataset. The purple solid line with shade area shows the trend of LWDR ($0.187 \pm 0.028\,\mathrm{W\,m^{-2}\,yr^{-1}}$) during the period 1960–2000 from WATCH dataset. The right panel shows the prior normal probability density function (PDF) with modeled mean and SD (black solid line) and posteiror normal PDF (red and purple dotted line) with given trend of LWDR from CRUNCEP and WATCH respectively.

TCD
9, 2301–2337, 2015

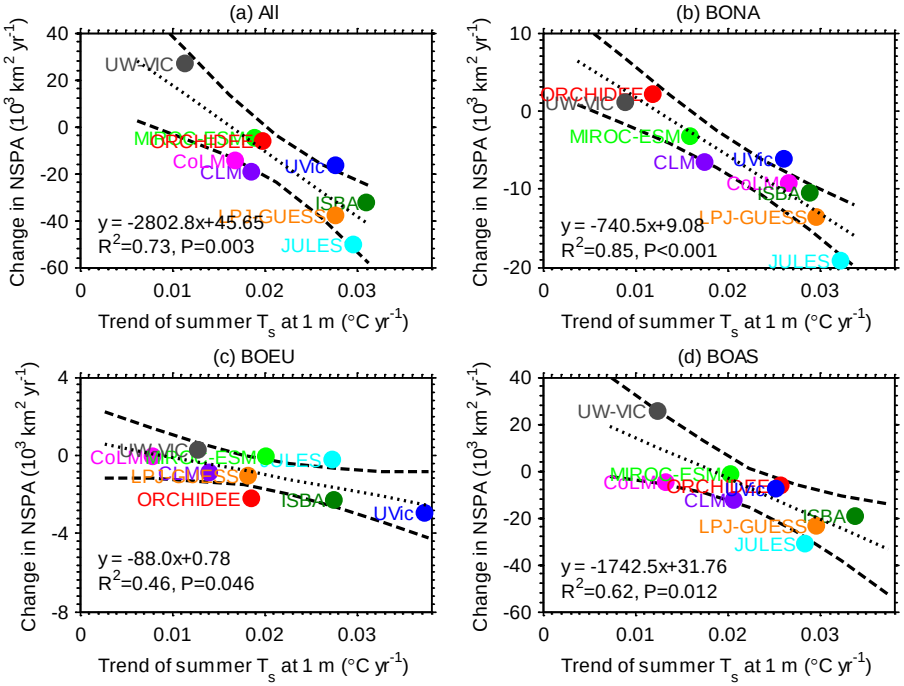

Figure 9. Simulated trends of summer T_s at 1 m and loss rate of NSPA over **(a)** boreal regions, **(b)** BONA, **(c)** BOEU and **(d)** BOAS across the nine models.

TCD
9, 2301–2337, 2015